catalysts

MDPI

Article

Ru/Beta Zeolite Catalysts for Levulinic Acid Hydrogenation: The Importance of Catalyst Synthesis Methodology

Oana Adriana Petcuta [1], Nicolae Cristian Guzo [1], Mihai Bordeiasu [1], Adela Nicolaev [2], Vasile I. Parvulescu [1] and Simona M. Coman [1,*]

[1] Department of Inorganic Chemistry, Organic Chemistry, Biochemistry and Catalysis, Faculty of Chemistry, University of Bucharest, Bdul Regina Elisabeta 4-12, 030016 Bucharest, Romania; oana.petcuta@s.unibuc.ro (O.A.P.); nicolae.guzo@s.unibuc.ro (N.C.G.); mihai.bordeiasu@s.unibuc.ro (M.B.); vasile.parvulescu@chimie.unibuc.ro (V.I.P.)

[2] National Institute of Materials Physics, Atomistilor 405b, 077125 Magurele-Ilfov, Romania; adela.nicolaev@infim.ro

* Correspondence: simona.coman@chimie.unibuc.ro

Abstract: Ruthenium-based catalysts were prepared through a deposition–precipitation approach, taking beta zeolites with Si/Al ratios of 12.5, 18.5, and 150, respectively, as supports, and 1–3 wt% loadings of metal. Their activation was performed in the presence of either H_2 or $NaBH_4$. The dispersion of the Ru species and the acid–base properties were influenced by both the preparation method and the activation protocol. The catalysts reduced under H_2 flow presented well-dispersed Ru(0) and RuO_x nanoparticles, while the reduction with $NaBH_4$ led to larger RuO_x crystallites and highly dispersed Ru(0). These characteristics exerted an important role in the hydrogenation of levulinic acid (LA) to γ-valerolactone (GVL). The H_2 dissociation occurred via a heterolytic mechanism involving Lewis acid–base pairs associated with RuO_x and the framework oxygen (Si-O-Al) located near the zeolite pore edge. The Ru(0) nanoparticles activated the –C=O bond of the LA substrate, while the presence of the carrier zeolite Brønsted acid sites promoted the ring-closure esterification of the 4-hydroxyvaleric acid (4-HVA) intermediate to GVL. An optimal combination of these features was achieved for the catalyst with 3 wt% Ru and a Si/Al ratio of 150, which selectively converted LA (X_{LA} = 96.5%) to GVL (S_{GVL} = 97.8%) at 130 °C and 10 bars of H_2.

Keywords: beta zeolite; ruthenium; deposition–precipitation; levulinic acid; catalytic hydrogenation; gamma-valerolactone

Academic Editor: De Fang

Received: 25 November 2024
Revised: 13 January 2025
Accepted: 14 January 2025
Published: 16 January 2025

Citation: Petcuta, O.A.; Guzo, N.C.; Bordeiasu, M.; Nicolaev, A.; Parvulescu, V.I.; Coman, S.M. Ru/Beta Zeolite Catalysts for Levulinic Acid Hydrogenation: The Importance of Catalyst Synthesis Methodology. *Catalysts* **2025**, *15*, 80. https://doi.org/10.3390/catal15010080

1. Introduction

Due to its importance, catalytic hydrogenation for biomass valorization is one of the most significant examples requiring an efficient and suitable catalyst design, which is still a significant challenge [1,2]. In most of the reported procedures, conversion occurs as a multistep reaction (e.g., C=O saturation ring-opening and C-O cleavage) in multiphase systems. Therefore, reaching high selectivity to a particular product in the presence of conventional catalysts is a major challenge [3].

In this context, the selective hydrogenation of levulinic acid (LA) provides a good example [4]. Most of the reported investigations have focused on LA conversion to γ-valerolactone (GVL), which is a valuable chemical used as an additive for biodegradable fuels, a monomer for bulk polymers, and a solvent. With this aim, previous studies have shown that noble-metal-based catalysts, such as Ru [5–11], Au [12], Pd [13], and Pt [14], are

preferrable. Among these, ruthenium-based catalysts exhibit the highest activities [15,16]. To further improve their catalytic efficiency, various materials, such as carbon, alumina, titania, lamellar zeolites (MWW zeolites), mesoporous polyamides, and metal organic frameworks (MOFs), have been used as carriers [17–23].

Owing to their unique porous structure, shape selectivity, and medium–strong acidity, zeolites are the most commonly used solid catalysts in the traditional chemical industry, and recently in biomass valorization [24,25]. Zeolites are also efficient carriers for the dispersion of active metal or metal oxide phases. The resulting materials combine the acidic properties of zeolites with the redox properties of metals, thus affording improved catalytic properties for the reactions involved in biomass conversion [3,25]. Therefore, one of the investigated efforts aiming to improve the catalytic activity of metal-based catalysts focuses on bifunctional catalysts combining ruthenium as the metal and zeolites as supports. These catalysts have previously been prepared using a common impregnation method [26–29]. However, this preparation method has shown limited performance for Ru catalysts in LA hydrogenation. Despite this, only few reports have focused on the deposition–precipitation (DP) approach as an alternative to the impregnation method for producing catalysts with high efficiency in LA hydrogenation [23]. Compared to the impregnation method, the DP approach, which is widely used for the synthesis of nanostructured materials, could provide another way to prepare more uniformly dispersed metal nanoparticle catalysts [30]. Simultaneously, mesopores can be generated via desilication in an alkaline environment, improving the mass transfer of reactants, intermediates, and products through the pore system of the carrier [31,32].

Among zeolites, beta zeolites serve as attractive supports for many important biomass valorization applications because of their characteristics such as large channels, strong acid sites, and high thermal and chemical stability [33]. However, previous studies have demonstrated basicity for zeolites in the H-form. The contribution of lattice oxygen atoms to acid-catalyzed reactions has been suggested, where reactions proceed in a concerted manner [34]. In other words, zeolite lattice oxygen atoms may operate as base sites in combination with Brønsted acid sites. Thus, the lattice oxygen adjacent to Al on H-form zeolites possesses basicity and participates in several acid-catalyzed reactions. More recently, Kondo and co-workers [35] associated such base sites with framework oxygen bridging the silicon and aluminum (Si-O-Al) at the external surface zeolite pore edge, with the site density dependent on the zeolite's topology.

To the best of our knowledge, the study of activation protocols coupled with the effect of the preparation approach on the structure and performance of zeolite-based Ru catalysts for LA hydrogenation has never been reported. Herein, we attempt to synthesize Ru/Beta zeolite catalysts (Si/Al = 12.5, 18.5, and 150) with loadings of metal of 1, 2, and 3 wt% Ru, respectively, using the DP approach, followed by their activation through either reduction in a molecular hydrogen flow or direct chemical reduction with $NaBH_4$ as the reagent. The catalytic performances of the synthesized catalysts will be investigated for LA hydrogenation in 1,4-dioxane as the solvent. This study will mainly focus on (i) the influence of the activation protocol upon the structure of the catalysts and the chemical state of the Ru species, and (ii) on insights into the performances of the redox and acid–base sites for LA hydrogenation to GVL.

2. Results and Discussion

2.1. Catalyst Characterization

Figure 1 shows the XRD patterns of the pristine beta zeolite carriers with Si/Al ratios of 12.5, 18.5, and 150. The characteristic reflections of BEA18.5 and BEA12.5 are sharper and more intense, indicating highly regular structures and slightly larger crystals associated

with the higher Al content [36]. Additionally, the reflection lines are shifted to lower 2θ values, indicating an increase in unit cell size that corresponds to an increase in Al-O bonds (1.91 Å) compared to Si-O ones (1.69 Å) [36].

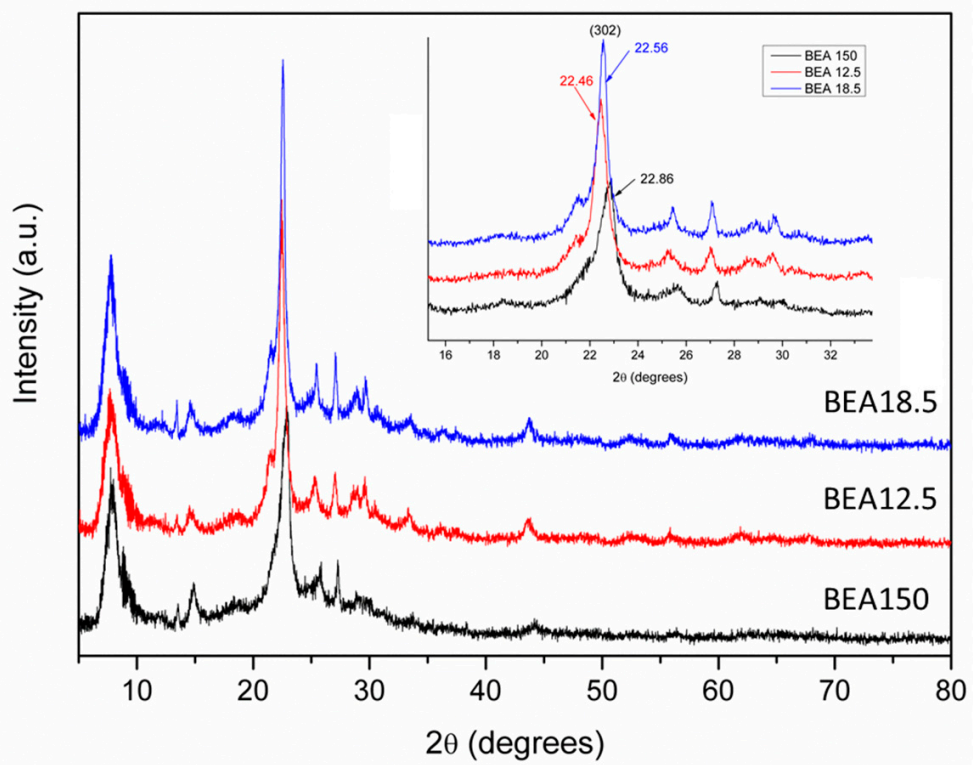

Figure 1. XRD patterns of pristine beta zeolites with different Si/Al ratios. Inset: XRD patterns of the BEA–zeolite samples in the 2θ = 16–30° range.

Further, the XRD patterns of the Ru/BEA catalysts preserved the typical diffraction lines of the beta zeolite carriers (Figure 2A–C). However, these showed an attenuation in their intensity, suggesting a partial loss of crystallinity.

The observed partial loss of crystallinity may be attributed to a desilication process occurring during the DP step. This is also consistent with the reports of Groen et al. [37], who suggested that the desilication of beta zeolites with a low Si/Al ratio (i.e., 12.5 and 18.5 in this work) is inhibited, owing to the relatively high concentration of Al (i.e., the negatively charged AlO_4^- tetrahedrons), which creates a more stable framework for the extraction of silicon. As an effect, the hydrolysis of the Si-O-Al bond in the presence of OH^- is hindered compared to the relatively easy cleavage of the Si-O-Si linkage in the absence of neighboring tetrahedra (i.e., BEA zeolite with a Si/Al ratio of 150).

The crystallinity of the Ru/BEA catalysts was determined by taking the highest intensity of the three characteristic lines of the beta zeolite carriers as a reference (i.e., 100% crystallinity). As Figure 1 shows, the crystallinity of the catalysts containing BEA12.5 and BEA18.5 carriers decreased to 83%, while that of Ru/BEA150 decreased to 59.7%. The advanced desilication of Ru/BEA150 is also confirmed by the shift in the reflection line at 2θ 22.86° (BEA150) to 22.57° (Ru/BEA150) (Figure 2C), which suggests an increase in the unit cell size due to the increased concentration of the longer Al-O bonds (1.91 Å). However, this process became even more prominent for the Ru/BEA catalysts subjected to reduction with $NaBH_4$ (i.e., 3Ru/BEA12.5-B, as illustrated in Figure 2A). In this case, the crystallinity of the beta zeolite support significantly decreased to 50.9%.

According to reports in the literature [23], during the DP approach, the formation of large metal nanoparticles is prevented by the gradual release of hydroxide ions and

the homogeneous precipitation of metal salt. However, the XRD patterns of the Ru/BEA catalysts (Figure 2A) revealed that the structure and, especially, the crystallite size of the ruthenium species are significantly influenced by reduction under a molecular hydrogen flow compared to chemical reduction with $NaBH_4$. As we have recently shown [38,39], Ru/BEA catalysts (1 and 3 wt% Ru and a Si/Al ratio of 12.5), prepared by a DP approach and activated by molecular hydrogen, were characterized by highly dispersed RuO_x species (not detectable in XRD patterns), alongside uniformly dispersed small metallic ruthenium particles. However, for these samples, it is difficult to calculate the size of the metallic ruthenium particles due to the ambiguous boundary of the characteristic diffraction lines. Thus, for the case of the 3Ru/BEA18.5, 2Ru/BEA150, and 3Ru/BEA150 catalysts, the size of the metallic ruthenium crystallites, calculated using the Debye–Scherrer Equation (2), ranged between 8 and 16 nm. Also, the formation of RuO_x species cannot be entirely ruled out. The absence of their characteristic diffraction lines from the recorded XRD patterns suggests either the presence of ruthenium oxide crystallites smaller than approximately 3 nm or the absence of this crystalline phase.

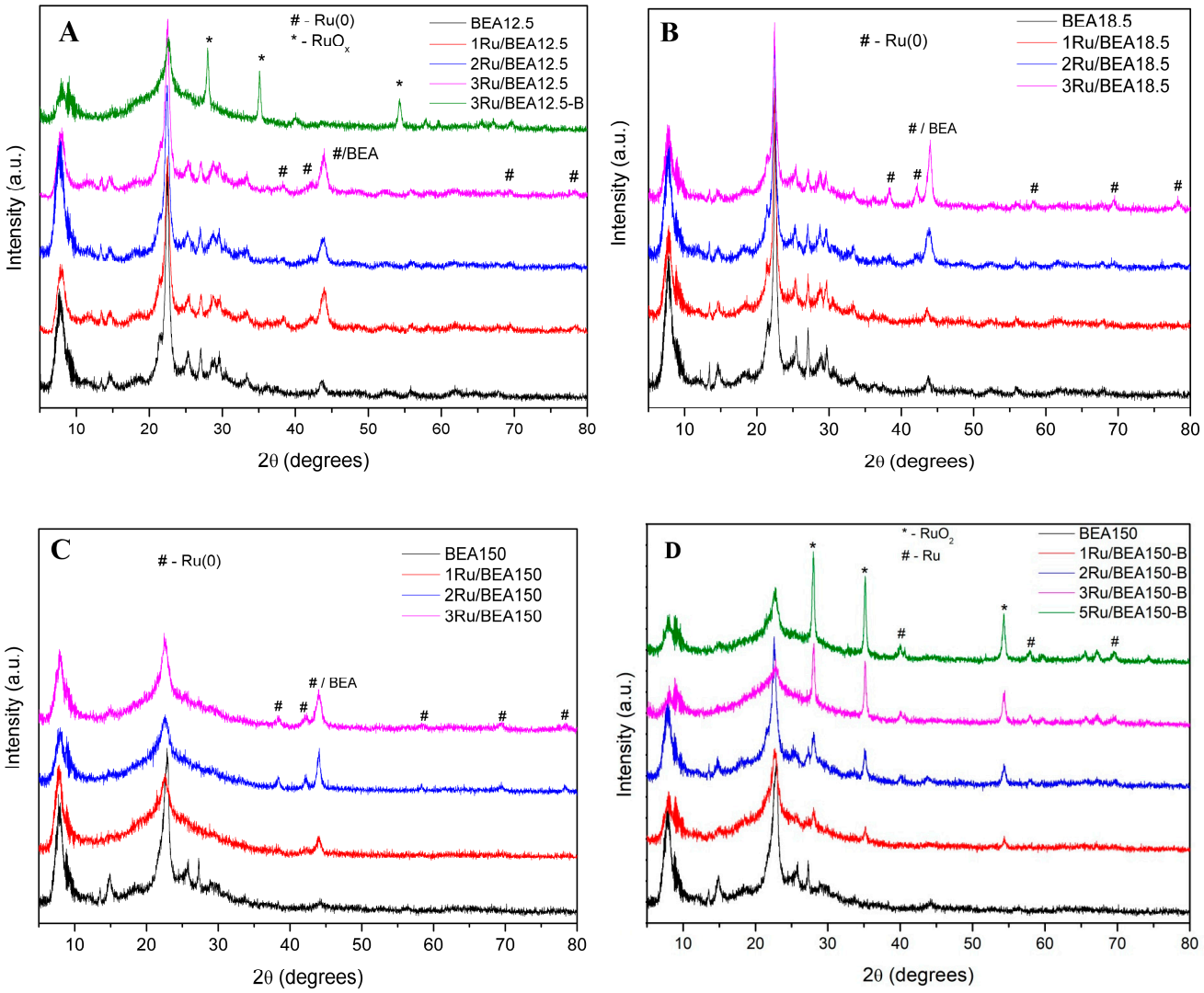

Figure 2. XRD patterns of (**A**) pristine BEA12.5 zeolite and Ru/BEA12.5 catalysts; (**B**) pristine BEA18.5 zeolite and Ru/BEA18.5 catalysts; (**C**) pristine BEA150 zeolite and Ru/BEA150 catalysts; and (**D**) pristine BEA150 zeolite and Ru/BEA150-B catalysts.

Contrarily to the reduction with hydrogen, the use of $NaBH_4$ promoted the formation of larger RuO_x crystallites (2θ = 28.1, 35.1, 44.0, and 54.4°, indexed to the (110), (101), (111), and (211) planes of anhydrous crystalline RuO_2 (ICDD-JCPDS Card No. 43-1027)). These appear to coexist with smaller metallic Ru(0) nanoparticles (Figure 2A,D). One possible explanation for the formation of larger RuO_x crystallites, measuring 15–16 nm in size, is the possible adsorption of borate species onto the ruthenium particles, generated through the hydrolysis of sodium borohydride. Also, in line with the findings of Liu et al. [40], this step may reduce the surface electron density and favor their aggregation.

The HR-XPS spectra of the Ru3d region for the 3Ru/BEA150 and 3Ru/BEA12.5-B catalysts are presented in Figure 3. In accordance with Balcerzak et al. [41], the spin–orbit split Ru3d doublet (i.e., Ru3d5/2 and Ru3d3/2) is resolved by applying a set of narrow (0.6–0.8 eV) symmetric components. For the 3Ru/BEA150 catalyst (Figure 3A), the Ru3d5/2 bands at 279.7 and 280.5 eV are attributed to metallic ruthenium and RuO_2, whereas for the 3Ru/BEA12.5-B catalyst (Figure 3B), the Ru3d5/2 bands are attributed to metallic ruthenium at 280.0 eV and RuOx at 281.7 eV. The Ru3d3/2 peak region is also populated with two ruthenium components, providing a fixed area ratio of the 3d5/2 to 3d3/2 corresponding components, equal to 3:2, and a constant value of their separation energy, equal to 4.15 eV. The C1s main C–C symmetric component is established at 284.6 eV to fully occupy the region envelope. An extra C1s component at 285.7 eV can be attributed to C-O bonds on the surface-adsorbed organic contaminants.

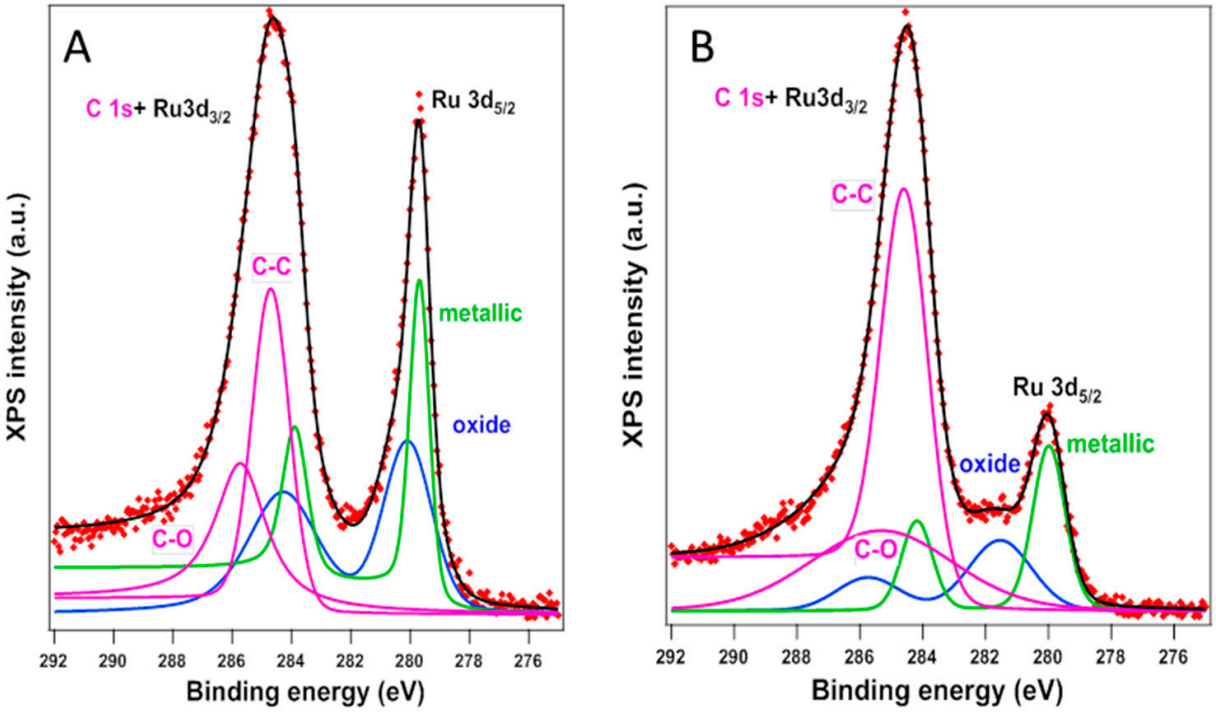

Figure 3. The XPS Ru3d spectra of 3Ru/BEA150 (**A**) and 3Ru/BEA12.5-B (**B**) catalysts.

It is worth noting that the reduction with molecular hydrogen preserved the RuOx species to a greater extent compared to the treatment with NaBH4, generating a higher reduction (Table 1, entries 2 and 4). However, these species were well dispersed in comparison with the large RuOx crystallites observed after the reduction with NaBH4 (XRD patterns, Figure 2A).

Table 1. Percentages and ratios of the Ru^0 and Ru^{x+} species, and the Si/Al ratio.

Catalysts	Ru3d		Ru^{x+}/Ru^0	Si/Al
	Ru^0, at%	Ru^{x+}, at%		
1Ru/BEA12.5 *	25.06	74.94	3.0	13.04
3Ru/BEA12.5 *	23.87	76.13	3.2	12.24
3Ru/BEA150	30.40	69.60	2.3	42.64
3Ru/BEA12.5-B	55.48	44.52	0.8	12.40

* Ref. [38].

The Si/Al ratio of the zeolite carrier also exhibited an important influence upon the nature of the ruthenium species. Thus, for the catalysts with Si/Al = 150, the percent of metallic ruthenium is higher compared to the samples with a Si/Al ratio of 12.5 (Table 1, entries 2 and 3). Also, a significant decrease in the Si/Al ratio from 150 to 42.55 (Table 1, entry 3) confirms, along with the XRD measurements, an advanced desilication of the BEA150 zeolite carrier during the DP approach. Changes also occurred in the surface loading of Na. While for the samples reduced by molecular hydrogen, a content of 1.0–1.22 at% Na (1072.2 eV) was evidenced, for 3Ru/BEA12.5-B, the XPS analysis indicated a higher surface loading of Na (16.28 at%) as Na[AlSi3O8] species, indicating an ion-exchange H^+/Na^+ process during the reduction step. No chlorine was evidenced, irrespective of the preparation procedure.

The N_2 adsorption–desorption isotherms of the Ru/BEA-150 catalysts are depicted in Figure 4, alongside the corresponding distribution of pore size (inset). According to the IUPAC classification, these isotherms correspond to a combination of typical Type IV and Type 3 (H3) hysteresis loops. These correspond to micropore filling at low pressures ($p/p_0 < 0.1$) and to hysteresis loops at higher pressures (p/p_0 of 0.45–0.90), illustrating a hierarchical porous system comprising both micro- and mesoporosity. In addition, near the saturation point (p/p_0 of 1.0), the N_2 adsorption–desorption isotherms also showed a sharp rise in the adsorbed amount, which is associated with condensation in the inter-particle voids (macropores).

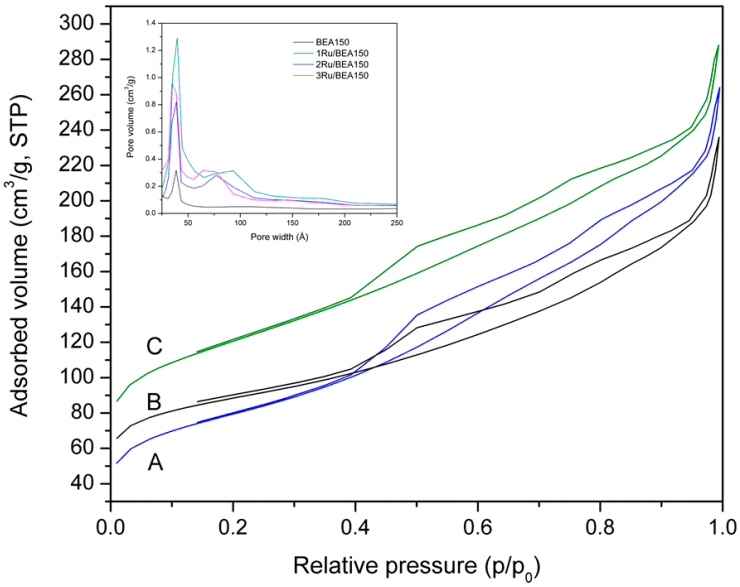

Figure 4. N_2 adsorption–desorption isotherms and pore size distribution profiles (BJH desorption data) of the representative supported Ru/BEA150 samples: 1Ru/BEA150 (**A**), 2Ru/BEA150 (**B**), and 3Ru/BEA150 (**C**).

The data compiled in Table 2 indicate that the deposition of ruthenium led to a decrease in surface area (Table 2, column 3). However, the micropore surface area (Table 2, column 5) experienced a more pronounced decline compared to the external surface (Table 2, column 4). This difference is attributed to the predominant deposition of the ruthenium species on the inner surface of the narrow zeolite pores. However, both the Langmuir and external (*t*-plot) surface areas of these catalysts confirm that the pores of the zeolite are only partly blocked.

Table 2. Textural properties of BEA and Ru/BEA samples.

Sample	S_{BET}, (m^2/g) *	S_{ext}, (m^2/g) **	S_{micro}, (m^2/g) **	V_{total}, (cm^3/g) ***	V_{meso}, (cm^3/g) ****	V_{micro}, (cm^3/g) *****	Pore Size Distribution, (nm) ******
BEA12.5	495	186	309	0.72	0.58	0.14	9.4; 31.5
1Ru/BEA12.5	415	168	247	0.65	0.54	0.11	9.3; 30.0
2Ru/BEA12.5	502	186	316	0.80	0.66	0.14	9.4; 31.5
3Ru/BEA12.5-B	262	172	90	0.38	0.34	0.04	4.0; 9.4
BEA150	497	133	364	0.29	0.12	0.17	3.8
1Ru/BEA150	281	217	64	0.35	0.32	0.03	3.9; 9.3
2Ru/BEA150	275	178	96	0.34	0.30	0.04	3.9; 7.7
3Ru/BEA150	421	273	148	0.38	0.31	0.07	3.9; 7.1

* Calculated by the BET method. ** External surface area calculated using the *t*-plot method. *** Total pore volume determined at a relative pressure (p/p_0) of 0.98. **** Mesopore volume calculated using the BJH method. ***** Micropore volume calculated using the *t*-plot method. ****** Mesopore diameter calculated using the BJH method.

The Ru/BEA catalysts also displayed the development of additional mesopores (Table 2, column 10), confirming a desilication process well correlated with the BEA Si/Al ratio. Thus, the external surface of Ru/BEA150 was significantly enlarged compared to that of the Ru/BEA12.5 catalysts (Table 2, column 4). This desilication process is consistent with the results of the XRD and XPS measurements.

2.2. Catalytic Activity

The Ru/BEA catalysts were evaluated during the hydrogenation of LA. Based on the fact that the kinetic diameter of LA is approximately 0.6 nm (6 Å) [42], and that its various intermediates and potential final products, including GVL, pentanoic acid, 1,2-pentandiol, and different hydrocarbons, have similar or smaller sizes, it was anticipated that the synthesized Ru/BEA zeolites developed through the DP approach (with abundant mesopores) would enhance the mass transport properties, thereby increasing the reaction efficiency.

For the hydrogenation of LA to GVL in water, alcohols, and alcohol/water mixtures, working with Ru catalysts supported on carbon, the literature highlights the significance of the reaction solvent [43,44]. Therefore, despite the limited solubility of hydrogen [45], water enhances the H-spillover effect on the catalyst surface [46], facilitating the adsorption of the reactant and reaction intermediates, thus leading to a faster reaction rate for LA and a higher yield of GVL [46,47]. However, the vulnerability of the zeolites' framework to the attack of the hot liquid water impedes their full utilization in aqueous phase processes. According to reports of Zhang et al. [48] the presence of hydrophilic moieties such as Brønsted acid sites (BAS), extra-framework Al, and silanol defects plays a crucial role influencing the zeolites' susceptibility to hot liquid water. Specifically, the density of the silanol defects has been found to be the most critical factor in this process. Moreover, the use of water as a solvent may also produce the hydrolysis of GVL to 4-hydroxy valeric

acid, which can be subsequently hydrogenated to 1,4-pentanediol [49]. Thus, in light of these findings, the reaction solvent 1,4-dioxane, i.e., a polar aprotic solvent with a polarity index of 4.8 (ε = 2.25), was selected. This solvent demonstrated the ability to enhance the stability of zeolites, while also providing the advantage of a significantly higher solubility for hydrogen [6]. It also allows work at a lower hydrogen pressure and practical benefits for the analysis of the reaction products [26,50].

The optimization of the reaction time and temperature was investigated for the 1Ru/BEA150 catalyst. At 10 bars of H_2 and 130 °C, the increase in the reaction time from 5 to 24 h led to a gradual increase in the conversion of LA, reaching 73.9% for a yield to GVL of 70.2% (S_{GVL} = 95.0%). Based on this, 24 h was established as a reference reaction time for further experiments. Then, the increase in the reaction temperature to 190 °C led to an increase in the conversion to 99.8%. However, due to the instability of 1,4-dioxane in the presence of acid catalysts at this temperature, the yield to GVL decreased to 79.5%, resulting in the formation of dioxane-derived byproducts, as also suggested by Luo et al. [26]. Based on these results, the optimal reaction temperature for further experiments was set to 130 °C.

Noteworthily, under these conditions, the selectivity to GVL was almost total. The only detected intermediate was 4-hydroxyvaleric acid (4-HVA). No intermediates, such as α-angelica lactone (α-AL) or GVL over-hydrogenation products (e.g., 1,4-pentanediol and valeric acid), were identified. The low amounts of 4-HVA may be related to a fast conversion of GVL, while the formation of α-AL requires an acid-catalyzed endothermic dehydration of LA at reaction temperatures higher than 180 °C. As the mass balance of the substrate and products (LA+GVL) was always higher than 93 % (determined by GC analysis), to compare the catalytic activity of the investigated catalysts, Table 3 compiles only the GVL yields.

Table 3. The influence of the support nature and ruthenium loading on catalytic activity and selectivity.

Catalyst *	X_{LA}, %	Y_{GVL}, %	S_{GVL}, %
1Ru/BEA12.5	3.9	3.6	93.3
2Ru/BEA12.5	4.9	4.6	94.0
3Ru/BEA12.5	5.4	5.1	95.0
3Ru/BEA12.5-B	0	-	-
1Ru/BEA18.5	7.9	7.4	94.0
2Ru/BEA18.5	10.5	10.1	96.1
3Ru/BEA18.5	15.1	14.5	96.3
1Ru/BEA150	73.9	70.2	95.0
2Ru/BEA150	87.6	84.1	96.0
3Ru/BEA150	96.5	94.4	97.8

* Reaction conditions: 116 mg (1 mmol) LA, 10 mg catalyst, 3.5 mL dioxane, 10 bar H_2, 130 °C, 24 h. Note: The difference in selectivity up to 100% is given by 4-hydroxyvaleric acid (4-HVA).

As Table 3 shows, the LA conversion was influenced by both the Ru loading and the Si/Al ratio of the zeolite carrier. Regardless of the Si/Al ratio, increasing the Ru loading from 1 to 3 wt% led to an increase in activity. Also, for the catalysts with the same loading of ruthenium, an increase in the conversion of LA was determined by increasing the Si/Al ratio from 12.5 to 150 (Table 3, entries 1–3). Across the Ru/BEA150 catalysts, the conversion of LA was in the range of 73.9–96.5% (Table 3, entries 8–10).

For both the most efficient catalyst (3Ru/BEA150, Table 3, entry 10) and the completely inactive one (3Ru/BEA12.5-B, Table 3, entry 4), the Ru^{x+}/Ru^0 ratio was less than 2.5

(Table 1, entries 3 and 4). So, the determined catalytic behavior is not strictly explained by the differences in the oxidation state of Ru, but also by differences in the size of the RuO_x crystallites. The larger ones (3Ru/BEA12.5-B) relate to a weaker metal–support interaction that, consequently, permeates a high probability of leaching during the reaction. A similar effect of the reduction step may be taken into consideration irrespective of the catalyst nature.

NH_3/CO_2-TPD measurements were conducted for the most efficient catalyst (i.e., 3Ru/BEA150), and the results were compared to those of the less effective ones (i.e., 1Ru/BEA18.5 and 3Ru/BEA12.5-B). For the investigated catalysts, the NH_3-TPD profiles showed different percentages of weak (50–200 °C, Table 4), medium (200–300 °C, Table 4,), and strong acid sites (300–400 °C, Table 4) (Figure 5A,B). Specifically, BEA12.5 and BEA18.5 (Figure 5A) exhibited three pronounced peaks at 103, 200, and 381 °C, indicating the presence of both weak and medium-strength acid sites. Following the ruthenium loading, the population of the weak acid sites was slightly declined, while the medium and strong acid sites (200 and 381 °C) disappeared. The latter were replaced by new medium-strength acid sites (peak at 248 °C) generated by the deposition of the RuO_x crystallites [51]. For the 3Ru/BEA150 catalyst, another peak was evidenced at 225 °C (Figure 5B).

Table 4. Acid–base properties of the 3Ru/BEA12.5-B, 3Ru/BEA150, and 1Ru/BEA18.5 catalysts, determined from NH_3/CO_2-TPD.

Sample	Acid Site Population, (μmols/g)			Total Acid Sites, (μmols/g)	Base Site Population, (μmols/g)			Total Base Sites (μmols/g)	Base–Acid Ratio
	Range of Temperature (°C)				Range of Temperature (°C)				
	50–200	200–300	300–400		100–200	200–400	>400		
BEA12.5	61.8	36.2 (200 °C)	10.2	98.3	50.0	-	-	50.0	0.51
3Ru/BEA12.5-B	60.8	24.2 (248 °C)	-	85.0	49.4	231.8 μ	43.9	325.0	3.82
BEA18.5	74.3	17.0 (200 °C)	15.8	107.1	60.2	-	-	60.2	0.56
1Ru/BEA18.5	71.2	51.7 (248 °C)	-	122.9	70.4	80.2	-	150.6	1.23
BEA150	158.9	-	-	158.9	68.4	18.2	-	86.6	0.54
3Ru/BEA150	133.4	95.5	-	228.9	194.4	118.5	-	312.9	1.37

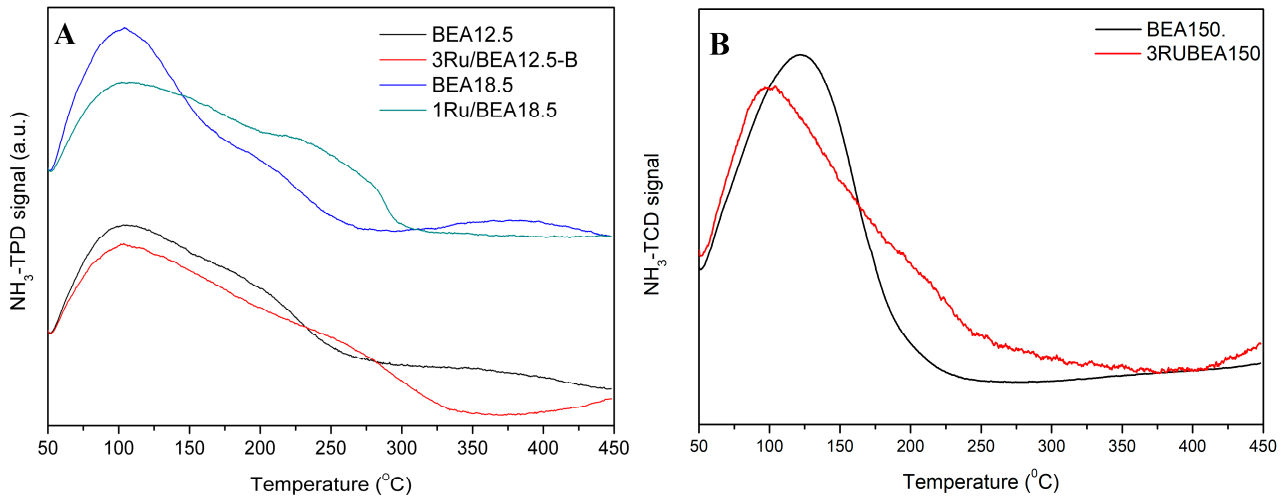

Figure 5. NH_3-TPD profiles for (**A**) 3Ru/BEA12.5-B, 1Ru/BEA18.5, and (**B**) 3Ru/BEA150 catalysts.

The CO_2-TPD profiles are depicted in Figure 6, and the surface features of the investigated samples are listed in Table 4. According to these profiles, the base sites can be classified into three categories: (i) weak base sites (100–200 °C), (ii) moderate-strength base sites (200–400 °C), and (iii) strong base sites (>400 °C) [52].

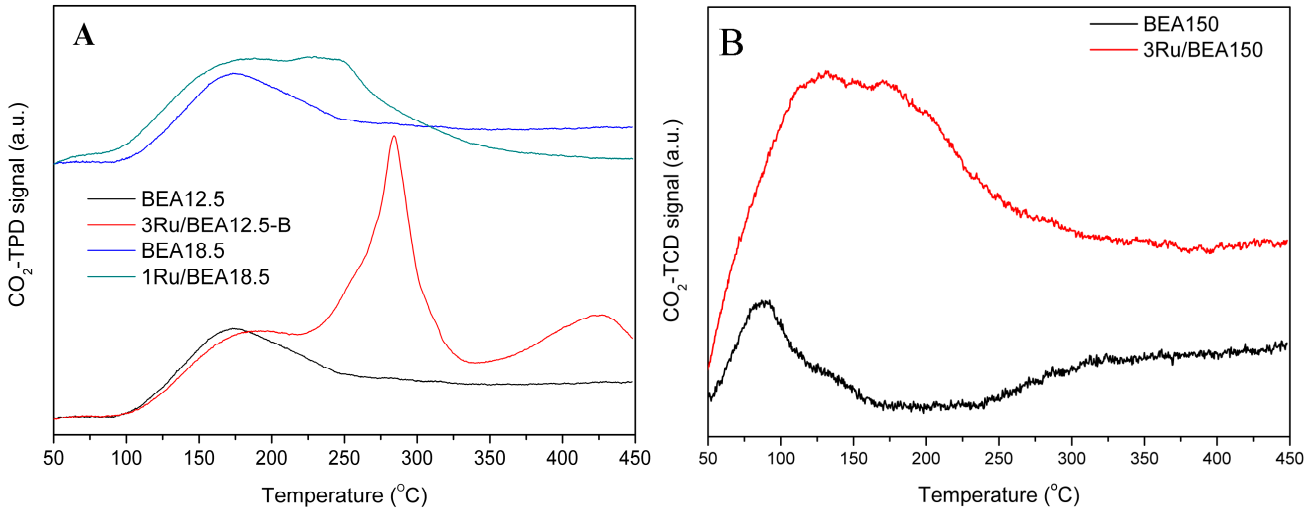

Figure 6. CO_2-TPD profiles for (**A**) 3Ru/BEA12.5-B, 1Ru/BEA18.5, and (**B**) 3Ru/BEA150 catalysts.

In our example, these new generated base sites with moderate strength (200–400 °C; 60.2 µmols/g CO_2 for 1Ru/BEA18.5 and 312.9 µmols/g for 3Ru/BEA150; Figure 6A,B and Table 4) can be associated with partial desilication, as also evidenced by the XRD and XPS measurements. As an effect, in accordance with the extent of desilication, new framework oxygen bridging the silicon and aluminum (Si-O-Al) was generated, which—in agreement with Kondo [35]—represents the basic lattice oxygen in H-BEA zeolite carriers. For 3Ru/BEA12.5-B, the CO_2-TPD profile revealed the presence of moderate-strength and strong base sites. The base strength of H-form zeolites is far weaker than that of conventional solid–base catalysts (alkali-cation-exchanged zeolites and metal oxides). Therefore, while the moderate-strength sites were attributed to the partial loss of zeolite crystallinity as an effect of the desilication, the strong base sites were attributed to the retention of Na^+ as a counter cation, balancing the negative charge of the aluminum tetrahedron during the reduction with $NaBH_4$ [53].

Previous studies suggested two different pathways for the production of GVL from LA [11,23]. These proposed (i) the hydrogenation of LA to 4-HVA, followed by dehydration to the GVL product (pathway 1, Scheme 1), and (ii) the acid-catalyzed endothermic dehydration of LA (temperatures higher than 180 °C) to α-AL via intra-molecular esterification, followed by hydrogenation to GVL (pathway 2, Scheme 1) [11,23]. However, the results collected in this study fit pathway 1, with 4-HVA serving as the intermediate (Scheme 1).

According to this, by hydrogenation, the keto functionality of LA is transformed into an alcohol group, resulting in the formation of the 4-HVA intermediate. This step can be achieved through either homo- [23] or heterolytic [11] H_2 dissociation.

While metallic ruthenium nanoparticles typically favor the homolytic dissociation of H_2 [54], in the case of the surface RuO_x species, due to their involvement in hydrogenation reactions, the mechanism of the reaction of the carbonyl group may be more complicated [15]. The support is not a spectator in this reaction. As previously shown in the hydrogenation of α,β-unsaturated aldehydes, an important effect upon the chemoselectivity to allylic alcohol is given by the existence of the Lewis acid site in the vicinity of the Ru(0) particles, which favors the heterolytic splitting of molecular hydrogen in hydride–proton

pairs [55]. In line with these findings, this study revealed the synergistic effect of Ru(0) nanoparticles activating the -C=O bond of the LA substrate and the Lewis acid–base pairs, which facilitated the heterolytic dissociation of H_2 into H^- and H^+. Specifically, the Lewis base, associated with the framework oxygen bridging the silicon and aluminum (Si-O-Al) situated near the zeolite pore edge on its external surface, can accept the generated protons, leaving the hydrides to the RuO_x (Lewis acid sites) (Figure 7). However, a homolytic mechanism for H_2 dissociation into 2H is also possible for metallic Ru nanoparticles.

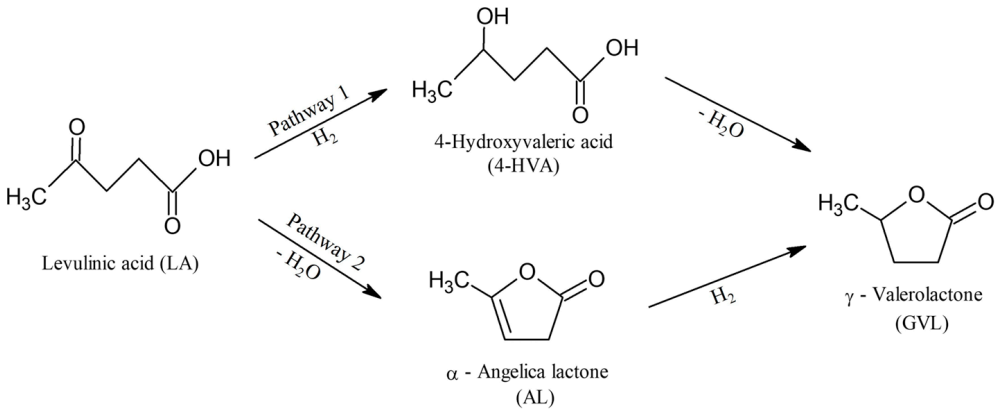

Scheme 1. Reaction pathways for the synthesis of GVL from LA.

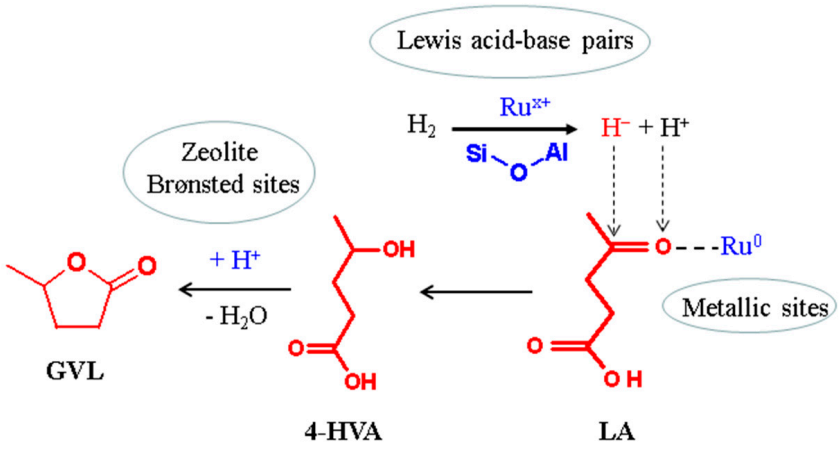

Figure 7. The proposed selective hydrogenation mechanism of LA to GVL through the heterolytic dissociation of H_2.

Following the conclusions of Ruppert et al. [56], the 4-HVA molecule, once formed, may undergo dehydration onto the Brønsted acid sites of the zeolite carrier. As a consequence, the GVL cyclic ester product is generated through a favorable intramolecular esterification process. Thus, the very high efficiency of 3Ru/BEA150 may be attributed to the optimal combination of the catalytic phase, which boasts a balanced Ru^{x+}/Ru^0 ratio of 1.3 (as determined by XPS), with the acid–base properties of the zeolite carrier provided by the Brønsted acid and bridged oxygen Lewis base sites.

Recyclability tests were conducted on the 3Ru/BEA150 catalyst, which displayed the highest catalytic efficiency. After 24 h, the catalyst was separated, washed, dried, and then utilized for another catalytic batch under identical reaction conditions. This process was repeated for five consecutive cycles. As illustrated in Figure 8, the catalyst maintained a high catalytic efficiency for five cycles, with only a slight deactivation in terms of the GVL production after the fourth cycle.

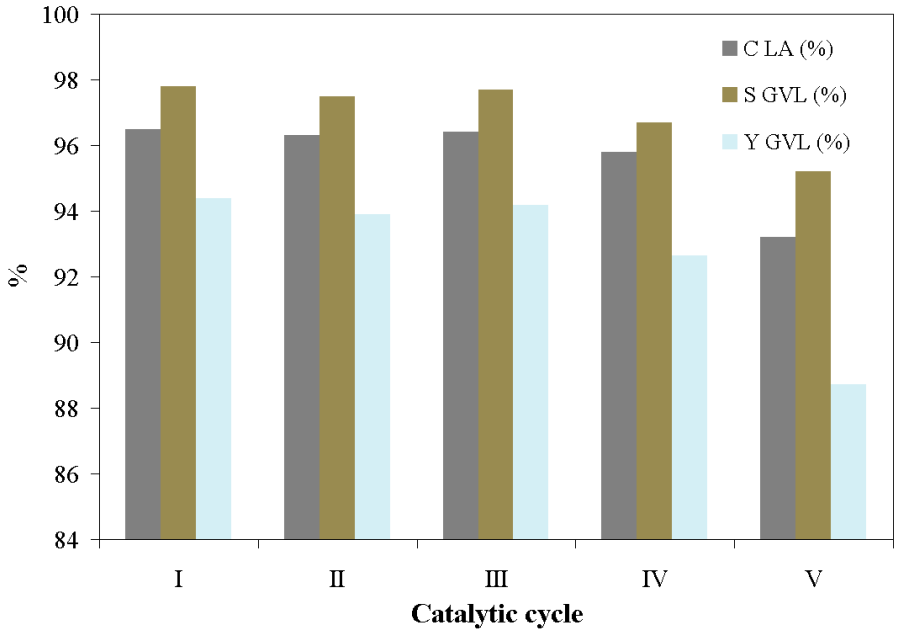

Figure 8. Recycling tests for 3Ru/BEA150 catalyst (1 mmol LA, 10 mg cat, 10 bar H_2, 130 °C, 24 h).

The stability of the investigated catalyst was further validated by the X-ray diffraction patterns (Figure 9) and infrared spectra (Figure 10) collected from both the fresh cycle and after the fifth cycle test.

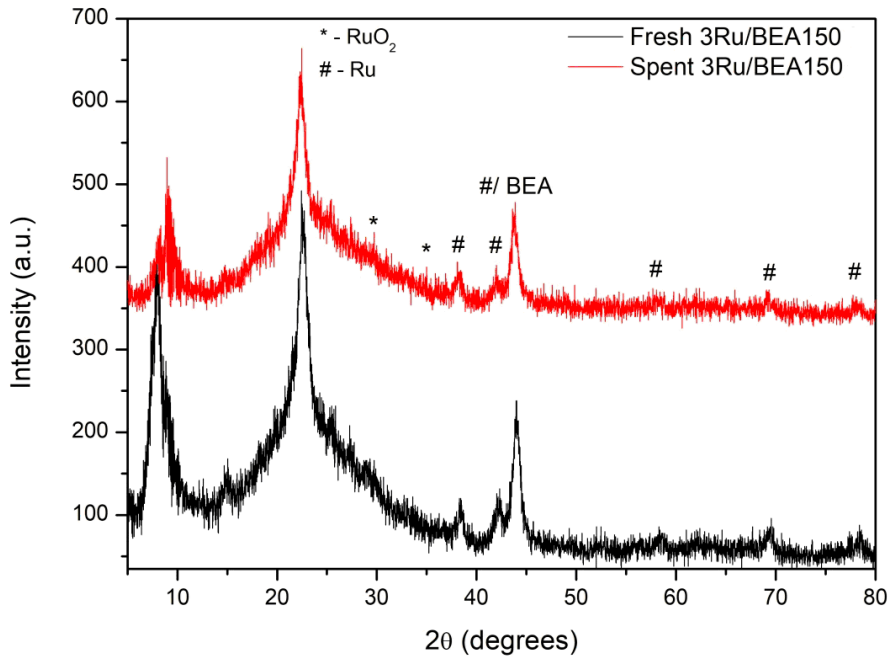

Figure 9. XRD patterns of the fresh and fifth cycles of the tested 3Ru/BEA150 catalyst.

The presence of lines characteristic of both the zeolite and Ru species in the DRIFT spectra after five recycling steps attests the high stability of the catalyst. However, the appearance of new bands in the 2750–3000 cm^{-1} region suggests the adsorption of organic molecules during the reaction, which is likely the primary cause of the gradual decline in catalyst efficiency after multiple catalytic cycles.

A stable and efficient bifunctional Ru/BEA catalyst was developed through the DP method and activation with molecular hydrogen, integrating the necessary catalytic characteristics for the LA conversion to GVL.

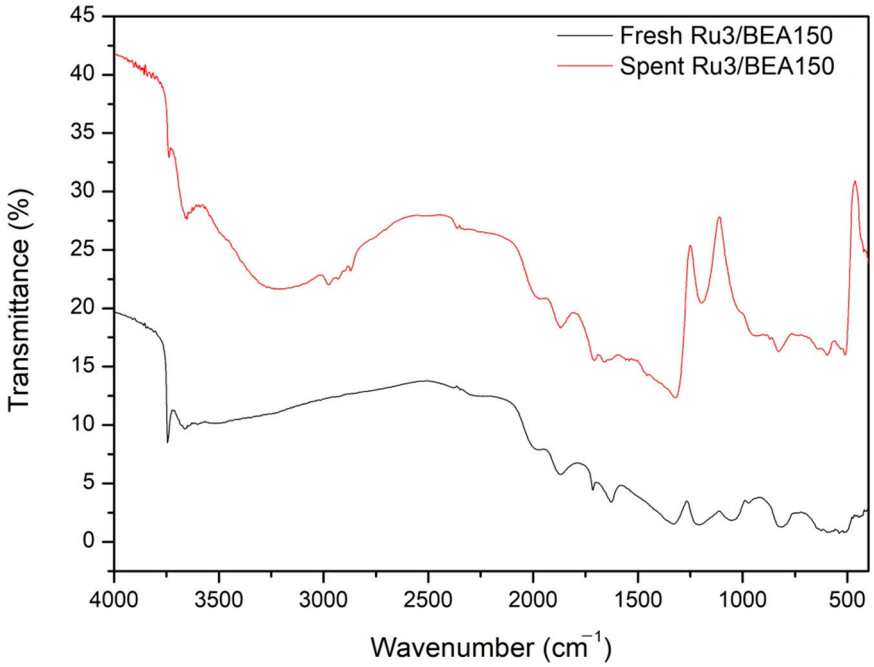

Figure 10. DRIFT spectra for the fresh and fifth cycles of the tested 3Ru/BEA150 catalyst.

Contrarily, the 3Ru/BEA12.5-B catalyst showed complete inactivity in the LA hydrogenation (Table 3, entry 4). This is attributed to the lack of catalyst stability, as proven by the XRD pattern of the spent catalyst (Figure 11). It shows no lines characteristic of RuO_x or metallic Ru(0) species.

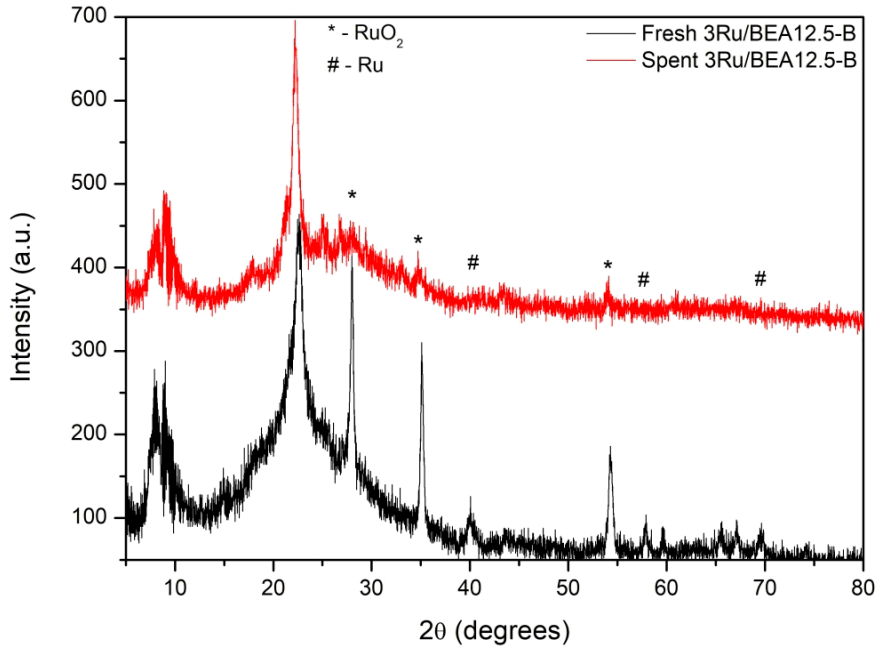

Figure 11. XRD patterns of fresh and 1st cycle of spent 3Ru/BEA12.5-B catalyst.

Therefore, it is likely that the primary cause for the rapid deactivation of the catalyst in LA conversion is an inadequate metal–support interaction. This is also confirmed by the

leaching of ruthenium species observed by UV-Vis spectroscopy (Figure 12), which revealed the presence of cationic ruthenium species in the reaction solution after the separation of the 3Ru/BEA12.5-B catalyst. The spectrum of $RuCl_3$ solution exhibits two signals: one located at 532 nm, assigned to a $\pi \rightarrow \gamma_5$ charge transfer, and the second one at 240 nm, due to the $\pi \rightarrow \gamma_3$ charge transfer typical of low-spin d complexes [57]. An absorption band around 360 nm also appeared in the spectrum due to the formation of $[RuCl_n(H_2O)_{6-n}]^{3-n}$ species. The UV-Vis spectra of the blank reaction (in the absence of the catalyst) indicate the presence of only levulinic acid (LA), with a maximum absorbance at 265 nm.

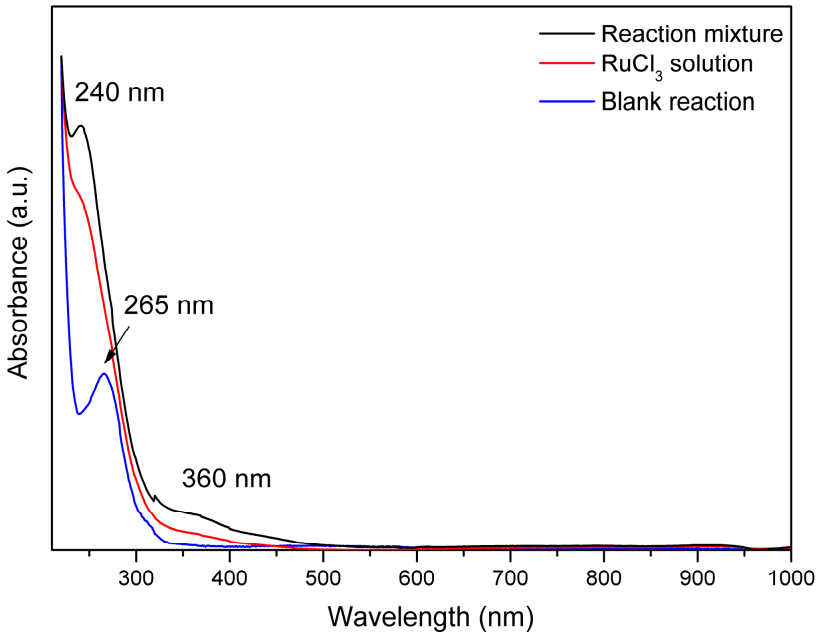

Figure 12. UV-Vis spectra of the aqueous $RuCl_3 \cdot 3H_2O$ solution, the reaction solution after the 1st cycle of the tested 3Ru/BEA12.5-B catalyst, and the reaction solution after blank reaction.

A significant proportion of H^+ acid sites were also lost due to an H^+/Na^+ ion-exchange process occurring during the catalyst reduction with the $NaBH_4$ reagent. This behavior was also proven by XPS and CO_2-TPD characterizations.

3. Materials and Methods

All chemicals and reagents were of analytical grade, purchased from Sigma-Aldrich (Saint Louis, MO, USA), and used without further purification.

3.1. Catalyst Preparation

Ru/BEA zeolite (Si/Al = 12.5, 18.5, and 150) catalysts with 1, 2, and 3 wt%Ru were synthesized by a deposition–precipitation (DP) method. In agreement with our previous work [38,39], in a typical preparation approach for the synthesis of the 1 wt% Ru-BEA catalyst, a solution of 26.1 mg $RuCl_3 \cdot 3H_2O$ (0.1 mmoles of $RuCl_3 \cdot 3H_2O$ in 60 mL H_2O) was added to a suspension of zeolite (1 g in 80 mL of H_2O) under stirring. Subsequently, a solution of NaOH (0.1 M) was added drop-wise until the pH reached 10. The mixture was then stirred for 24 h at room temperature. The same procedure was used to prepare catalysts with 2 and 3 wt% Ru. The Ru loading was adjusted by controlling the amount of the zeolite powder and the volume of the aqueous solution of $RuCl_3 \cdot 3H_2O$. The obtained solids were separated by centrifugation (6000 rpm for 35–40 min) and washed with an $AgNO_3$ reagent until a neutral pH was reached and until chlorine anions were absent from the rinse water. After washing, the catalysts were dried under vacuum at 110 °C.

The catalysts were then activated by calcination at 300 °C, for 4 h, followed by reduction with molecular hydrogen under a flow (H_2) (50 mL/min at 350 °C for 1 h, with a heating rate of 1 °C/min in a flow reactor). The obtained samples were denoted as xRu/BEAy, where x denotes the Ru content (1, 2 or 3 wt%) and y is the Si/Al ratio (12.5, 18.5, or 150).

For comparison, some Ru/BEA catalysts were directly reduced with $NaBH_4$ at room temperature. After drying, a portion of the recovered solid powder was added to 100 mL of a $NaBH_4$ ethanol solution (0.4 M), and the resulting mixture was stirred until bubble generation ceased (~4 h). The obtained catalysts were then separated from the solution by vacuum filtration, washed with deionized water until they reached a pH of ~7, then washed with 50 mL of ethanol, and finally dried at 110 °C overnight. The obtained catalysts are denoted as xRu/BEAy-B.

3.2. Catalyst Characterization

The synthesized Ru/BEA catalysts were characterized by X-ray diffraction (XRD), the adsorption–desorption of nitrogen at −196 °C, IR diffuse reflectance with Fourier transform (DRIFT) spectroscopy, NH_3/CO_2-TPD, and X-ray photoelectron spectroscopy (XPS). Powder X-ray diffraction (XRD) patterns were collected using a Shimadzu XRD-7000 apparatus with a Cu Kα monochromatic radiation of 1.5406 Å, 40 kV, and 40 mA at a scanning rate of 0.1 degree min^{-1} in the 2θ range of 5°–80°. The crystallinity of the samples was defined on the basis of the three characteristic diffraction lines of beta zeolite at Bragg angles of 7.6°, 21.2°, and 22.4°, and calculated using Formula (1) [58]:

$$\%Crystallinity = \frac{\sum_{i=1}^{3} intensity_i}{\left[\sum_{i=1}^{3} intensity_i\right] Ref} \times 100 \quad (1)$$

The average size of the metallic Ru crystallites in the Ru/BEA samples was determined using the Debye–Scherrer Equation (2) [59], taking the (002) reflection of Ru (2θ = 42.3°).

$$d = \frac{k\lambda}{\beta cos\theta} \quad (2)$$

where d is the crystallite size in nm; k = 0.94; λ is the wavelength of the X-ray (1.54178 Å); θ is the half-diffraction angle; and β is the full width at half maximum (FWHM) in radians at 2θ = 42.3°.

Textural characteristics (surface area, pore volume, and pore diameter) were determined from the nitrogen adsorption–desorption isotherms at −196 °C using a Micromeritics ASAP 2020 Surface Area and Porosity Analyzer (Micromeritics, Norcross, GA, USA). Prior to adsorption, all samples were systematically degassed at 200 °C under primary vacuum for 4 h. The surface area was calculated from the BET equation and the pore size distribution was determined based on the Barret–Joyner–Halenda (BJH) approach (Stone, UK), considering the desorption curves. DRIFT spectra were recorded and collected using a Bruker (Billerica, MA, USA) Tensor-II FTIR spectrometer at room temperature at a 4 cm^{-1} resolution in the range of 400–4000 cm^{-1}, and the final spectrum was obtained by averaging 32 scans. UV-vis spectra were recorded with a SPECORD 250-222P108 (Analytical Jena GmbH. KG, Jena, Germany) in the range of 200–1100 nm with a scan rate of 50 nm per second. CO_2- and NH_3-TPD measurements were performed using an AutoChem II 2920 station (Osaka, Japan). The samples (100−200 mg), placed in a U-shaped quartz reactor with an inner diameter of 0.5 cm, were pretreated under He (purity 5.0) at 120 °C for 1 h, and then exposed to a flow of CO_2 or a flow of NH_3 (1 vol%) in helium for 1 h. Subsequently, the samples were purged with a flow of He (50 mL × min^{-1}) for 20 min at 25 °C in order to

remove the weakly adsorbed species. TPD measurements were then started with a heating rate of 10 °C × min^{-1} up to 500 °C, where they were maintained for 30 min. The desorbed products were analyzed using GC-TCD chromatography. The amount of desorbed CO_2/NH_3, expressed as mmol of CO_2/NH_3 per gram of catalyst, was determined using a calibration curve. The X-ray photoelectron spectroscopy (XPS) analysis was performed on an AXIS Ultra DLD (Kratos Surface Analysis) setup (Kratos Analytical, Manchester, UK) using Al Kα1 (1486.74 eV) radiation produced by a monochromatized X-ray source at an operating power of 144 W (12 kV × 12 mA). The base pressure in the analysis chamber was ~1 × 10^{-9} mbar. XPS was performed to determine the surface chemical composition of the samples. All core-level spectra were deconvoluted using Voigt functions, singlets, or doublets (Lorentzian and Gaussian widths), with a distinct inelastic background for each component [60,61]. The minimum number of components was used to obtain a convenient fit. The binding energy scale was calibrated to the C 1 s standard value of 284.6 eV.

3.3. Catalytic Tests

The catalytic experiments were carried out in a stainless-steel autoclave (8 mL, HEL Instruments) under the following conditions: 116 mg of LA (1 mmol), 10 mg of the catalyst, and 3.5 mL of 1,4-dioxane. The system was flushed thrice with hydrogen and then pressurized to 10 bar. To exclude the influence of the external mass transfer limitations, the resulting mixture was stirred at a speed of 1200 rpm. The experiments were performed at 110–190 °C for 5–24 h. After the reaction, the autoclave was quickly cooled to room temperature, the catalyst was separated from the liquid phase by centrifugation (6000 rpm for 5 min), and the products were concentrated under vacuum at 60 °C.

The recovered products were silylated with 150 µL of a derivatization agent (N,O-bis (trimethylsilyl)trifluoroacetamide (BSTFA) with 1% trimethylchlorosilane (TMCS)) and 200 µL pyridine at 50 °C for 2 h. Afterwards, the obtained products were diluted with ethyl acetate (20 µL sample in 15 µL ethyl acetate) and analyzed by a Shimadzu gas chromatograph equipped with a flame-ionization detector (GC-FID) and a DB-5ms GC column (50 m × 0.2 mm × 0.33 µm) with a stationary phase composition of 5% diphenyl and 95% dimethylpolysiloxane. All samples were analyzed in triplicate. Product identification was performed using a Thermo Fischer Scientific (Waltham, MA, USA) Trace 1310 gas chromatograph coupled with an ISQ LT single-quadrupole mass spectrometer (GC-MS) equipped with a TG-5SILMS column (30 m × 0.25 mm × 0.25 µm).

LA conversion (X) and the selectivity to the reaction products (S_n) were calculated from the GC-FID chromatographic analysis using the following Equations (3):

$$X\% = \frac{n_i - n_t}{n_i} \times 100 \qquad S_n\% = \frac{Yield_n}{X} \times 100 \tag{3}$$

where n_i is initial moles of LA and n_t is moles of untransformed LA at time "t", as determined from the GC analysis.

4. Conclusions

In this study, Ru/BEA bifunctional catalysts were prepared by the deposition–precipitation (DP) method, and subsequently reduced with either molecular hydrogen or the $NaBH_4$ reagent. The characterization of the resulting catalysts demonstrated the formation of a hierarchically porous texture with both micro- and mesopores, limiting the steric and diffusional phenomena for both the substrate LA and reaction intermediates. The resulting hierarchical porosity made a significant part of the mesopore/external surface available, allowing a larger dispersion of the active catalytic phase.

The catalytic tests confirmed that the efficiency of Ru/BEA catalysts in LA hydrogenation is influenced by the activation protocol. For the activation with molecular hydrogen, the presence of highly dispersed Ru(0) nanoparticles and RuO_x crystallites led to a synergistic effect, converting LA into the 4-HVA intermediate, which further underwent dehydration to GVL on the Brønsted acid sites provided by the zeolite carrier. While it is not entirely ruled out that a homolytic dissociation of hydrogen could occur over metallic ruthenium nanoparticles, the presence of Lewis acid sites, such as RuO_x, and a high concentration of basic sites in the zeolite carrier, such as framework oxygen bridging the silicon and aluminum (Si-O-Al) at the external surface zeolite pore edge, suggest a possible heterolytic splitting of molecular hydrogen into hydride–proton pairs. However, it was proven that regardless of the hydrogen mechanism of dissociation, the presence of metallic ruthenium is essential for the activation of LA through the adsorption of carbonyl -C=O bonds.

The 3Ru/BEA150 catalyst demonstrated an exceptional ability to convert LA, achieving a conversion rate of 96.5% and a selectivity of 97.8% for GLV at 130 °C under 10 bars of H_2. This catalyst exhibited remarkable stability in the liquid phase, being efficient after five consecutive catalytic cycles without any significant change. The notable catalytic behavior that simultaneously provides high efficiency and stability at the same time in LA hydrogenation to GVL is, therefore, the result of the development of a tailor-made 3Ru/BEA150 catalyst with a combination of certain metallic/acid–base properties and a hierarchical micro/mesoporous structure.

The use of $NaBH_4$ in the reduction of the catalysts led to the formation of larger RuO_x crystallites and highly dispersed metallic Ru nanoparticles (i.e., 3Ru/BEA12.5-B, Ru/BEA150-B). The presence of such large particles suggests a weak metal–support interaction, which led to significant leaching during the reaction. Additionally, the high concentration of basic Na^+ sites on the zeolite carrier can be attributed to an ion-exchange H^+/Na^+ process during the chemical reduction. These two factors are likely responsible for the lack of catalytic efficiency observed in the studied synthesis.

Author Contributions: Conceptualization, O.A.P. and S.M.C.; methodology, O.A.P. and S.M.C.; validation, N.C.G., M.B. and A.N.; formal analysis, O.A.P. and A.N.; investigation, N.C.G., M.B. and A.N.; writing—original draft preparation, S.M.C.; writing—review and editing, V.I.P.; visualization, V.I.P. and S.M.C.; supervision, S.M.C.; funding acquisition, S.M.C. and N.C.G. All authors have read and agreed to the published version of the manuscript.

Funding: This research was funded by The Romanian Ministry of Research and Digitalization, grant number PNRR-III-C9-2022-I5-18, ResPonSE-Project, No. 760010/2022.

Data Availability Statement: The original contributions presented in this study are included in the article. Further inquiries can be directed to the corresponding author(s).

Acknowledgments: N.C.G. kindly acknowledges the Council of Doctoral Studies (C.S.U.D), University of Bucharest, Romania, for partial financial support.

Conflicts of Interest: The authors declare no conflicts of interest.

References

1. Li, N.; Wang, W.; Zheng, M.; Zhang, T. General Reaction Mechanisms in Hydrogenation and Hydrogenolysis for Biorefining. In *Catalytic Hydrogenation for Biomass Valorization*; Rinaldi, R., Ed.; RSC: London, UK, 2015; pp. 22–52.
2. Lazaridis, P.; Karakoulia, S.; Teodorescu, C.; Apostol, N.; Macovei, D.; Panteli, A.; Delimitis, A.; Coman, S.; Parvulescu, V.; Triantafyllidis, K. High hexitols selectivity in cellulose hydrolytic hydrogenation over platinum (Pt) vs. ruthenium (Ru) catalysts supported on micro/mesoporous carbon. *Appl. Catal. B* **2017**, *214*, 1–14. [CrossRef]
3. Sudarsanam, P.; Zhong, R.; Van den Bosch, S.; Coman, S.M.; Parvulescu, V.I.; Sels, B.F. Functionalised heterogeneous catalysts for sustainable biomass valorisation. *Chem. Soc. Rev.* **2018**, *47*, 8349–8402. [CrossRef]

4. Jin, X.; Yin, B.; Xia, Q.; Fang, T.; Shen, J.; Kuang, L.; Yang, C. Catalytic Transfer Hydrogenation of Biomass-Derived Substrates to Value-Added Chemicals on Dual-Function Catalysts: Opportunities and Challenges. *ChemSusChem* **2019**, *12*, 71–92. [CrossRef]
5. Alonso, D.M.; Wettstein, S.G.; Dumesic, J.A. Gamma-valerolactone, a sustainable platform molecule derived from lignocellulosic biomass. *Green Chem.* **2013**, *15*, 584–595. [CrossRef]
6. Tan, J.; Cui, J.; Deng, T.; Cui, X.; Ding, G.; Zhu, Y.; Li, Y. Water-Promoted Hydrogenation of Levulinic Acid to γ-Valerolactone on Supported Ruthenium Catalyst. *ChemCatChem* **2015**, *7*, 508–512. [CrossRef]
7. Wright, W.R.H.; Palkovits, R. Development of Heterogeneous Catalysts for the Conversion of Levulinic Acid to γ-Valerolactone. *ChemSusChem* **2012**, *5*, 1657–1667. [CrossRef] [PubMed]
8. Deng, J.; Wang, Y.; Pan, T.; Xu, Q.; Guo, Q.-X.; Fu, Y. Conversion of Carbohydrate Biomass to γ-Valerolactone by using Water-Soluble and Reusable Iridium Complexes in Acidic Aqueous Media. *ChemSusChem* **2013**, *6*, 1163. [CrossRef]
9. Piskun, A.S.; Van de Bovenkamp, H.H.; Rasrendra, C.B.; Winkelman, J.G.M.; Heeres, H.J. Kinetic modeling of levulinic acid hydrogenation to γ-valerolactone in water using a carbon supported Ru catalyst. *Appl. Catal. A* **2016**, *525*, 158–167. [CrossRef]
10. Wettstein, S.G.; Bond, J.Q.; Alonso, D.M.; Pham, H.N.; Datye, A.K.; Dumesic, J.A. RuSn bimetallic catalysts for selective hydrogenation of levulinic acid to γ-valerolactone. *Appl. Catal. B* **2012**, *117–118*, 321–329. [CrossRef]
11. Seretis, A.; Diamantopoulou, P.; Thanou, I.; Tzevelekidis, P.; Fakas, C.; Lilas, P.; Papadogianakis, G. Recent Advances in Ruthenium-Catalyzed Hydrogenation Reactions of Renewable Biomass-Derived Levulinic Acid in Aqueous Media. *Front. Chem.* **2020**, *8*, 221. [CrossRef]
12. Mustafin, K.; Cárdenas-Lizana, F.; Keane, M.A. Continuous Gas Phase Catalytic Transformation of Levulinic Acid to γ-Valerolactone over Supported Au Catalysts. *J. Chem. Technol. Biotechnol.* **2017**, *92*, 2221–2228. [CrossRef]
13. Feng, J.; Li, M.; Zhong, Y.; Xu, Y.; Meng, X.; Zhao, Z.; Feng, C. Hydrogenation of levulinic acid to γ-valerolactone over Pd@UiO-66-NH2 with high metal dispersion and excellent reusability. *Micropor. Mesopor. Mater.* **2020**, *294*, 109858. [CrossRef]
14. Nemanashi, M.; Noh, J.-H.; Meijboom, R. Hydrogenation of biomass-derived levulinic acid to γ-valerolactone catalyzed by mesoporous supported dendrimer-derived Ru and Pt catalysts: An alternative method for the production of renewable biofuels. *Appl. Catal. A* **2018**, *550*, 77–89. [CrossRef]
15. Michel, C.; Gallezot, P. Why Is Ruthenium an Efficient Catalyst for the Aqueous-Phase Hydrogenation of Biosourced Carbonyl Compounds? *ACS Catal.* **2015**, *5*, 4130–4132. [CrossRef]
16. Kasar, G.B.; Medhekar, R.S.; Bhosale, P.N.; Rode, C.V. Kinetics of Hydrogenation of Aqueous Levulinic Acid over Bimetallic Ru−Ni/MMT Catalyst. *Ind. Eng. Chem. Res.* **2019**, *58*, 19803–19817. [CrossRef]
17. Cao, W.; Luo, W.; Ge, H.; Su, Y.; Wang, A.; Zhang, T. UiO-66 derived Ru/ZrO_2@C as a highly stable catalyst for hydrogenation of levulinic acid to γ-valerolactone. *Green Chem.* **2017**, *19*, 2201–2211. [CrossRef]
18. Yan, L.; Yao, Q.; Fu, Y. Conversion of levulinic acid and alkyl levulinates into biofuels and high-value chemicals. *Green Chem.* **2017**, *19*, 5527–5547. [CrossRef]
19. Wang, Q.; Ling, X.; Ye, T.; Zhou, Y.; Wang, J. Ionic mesoporous polyamides enable highly dispersed ultrafine Ru nanoparticles: A synergistic stabilization effect and remarkable efficiency in levulinic acid conversion into γ-valerolactone. *J. Mater. Chem. A* **2019**, *7*, 19140–19151. [CrossRef]
20. Wojciechowska, J.; Jędrzejczyk, M.; Grams, J.; Keller, N.; Ruppert, A.M. Enhanced Production of γ-Valerolactone with an Internal Source of Hydrogen on Ca-Modified TiO_2 Supported Ru Catalysts. *ChemSusChem* **2019**, *12*, 639–650. [CrossRef] [PubMed]
21. Rivas, S.; Galletti, A.M.R.; Antonetti, C.; Licursi, D.; Santos, V.; Parajó, J.C. A Biorefinery Cascade Conversion of Hemicellulose-Free Eucalyptus Globulus Wood: Production of Concentrated Levulinic Acid Solutions for γ-Valerolactone Sustainable Preparation. *Catalysts* **2018**, *8*, 169. [CrossRef]
22. Guo, Y.; Li, Y.; Chen, J.; Chen, L. Hydrogenation of Levulinic Acid into γ-Valerolactone Over Ruthenium Catalysts Supported on Metal–Organic Frameworks in Aqueous Medium. *Catal. Lett.* **2016**, *146*, 2041–2052. [CrossRef]
23. Li, W.; Li, F.; Chen, J.; Betancourt, L.E.; Tu, C.; Liao, M.; Ning, X.; Zheng, J.; Li, R. Efficient and Sustainable Hydrogenation of Levulinic Acid to γ-Valerolactone in Aqueous Phase over Ru/MCM-49 Catalysts. *Ind. Eng. Chem. Res.* **2020**, *59*, 17338–17347. [CrossRef]
24. Jacobs, P.A.; Dusselier, M.; Sels, B.F. Will Zeolite-Based Catalysis be as Relevant in Future Biorefineries as in Crude Oil Refineries? *Angew. Chem. Int. Ed.* **2014**, *53*, 8621–8626. [CrossRef]
25. Sudarsanam, P.; Peeters, E.; Makshina, E.V.; Parvulescu, V.I.; Sels, B.F. Advances in porous and nanoscale catalysts for viable biomass conversion. *Chem. Soc. Rev.* **2019**, *48*, 2366–2421. [CrossRef]
26. Luo, W.; Deka, U.; Beale, A.M.; van Eck, E.R.H.; Bruijnincx, P.C.A.; Weckhuysen, B.M. Ruthenium-catalyzed hydrogenation of levulinic acid: Influence of the support and solvent on catalyst selectivity and stability. *J. Catal.* **2013**, *301*, 175–186. [CrossRef]
27. Abusuek, D.A.; Tkachenko, O.P.; Bykov, A.V.; Sidorov, A.I.; Matveeva, V.G.; Sulman, M.G.; Nikoshvili, L.Z. ZSM-5 as a support for Ru-containing catalysts of levulinic acid hydrogenation: Influence of the reaction conditions and the zeolite acidity. *Catal. Today* **2022**, *423*, 113885. [CrossRef]

28. Abusuek, D.A.; Nikoshvili, L.Z.; Sorokina, S.A.; Matveeva, V.G.; Sulman, M.G. Catalytic Hydrogenation of Levulinic Acid Using Ruthenium Dioxide Supported on Zeolites. *Chem. Eng. Trans.* **2021**, *88*, 277–282.
29. Piskun, A.; Winkelman, J.G.M.; Tang, Z.; Heeres, H.J. Support Screening Studies on the Hydrogenation of Levulinic Acid to γ-Valerolactone in Water Using Ru Catalysts. *Catalysts* **2016**, *6*, 131. [CrossRef]
30. Hu, L.; Wei, X.-Y.; Zong, Z.-M. Ru/Hβ catalyst prepared by the deposition-precipitation method for enhancing hydrodeoxygenation ability of guaiacol and lignin-derived bio-oil to produce hydrocarbons. *J. Energy Inst.* **2021**, *97*, 48–57. [CrossRef]
31. Feng, X.; Duan, X.; Cheng, H.; Qian, G.; Chen, D.; Yuan, W.; Zhou, X. Au/TS-1 catalyst prepared by deposition–precipitation method for propene epoxidation with H_2/O_2: Insights into the effects of slurry aging time and Si/Ti molar ratio. *J. Catal.* **2015**, *325*, 128–135. [CrossRef]
32. Wang, Z.; Brouri, D.; Casale, S.; Delannoy, L.; Louis, C. Exploration of the preparation of Cu/TiO_2 catalysts by deposition–precipitation with urea for selective hydrogenation of unsaturated hydrocarbons. *J. Catal.* **2016**, *340*, 95–106. [CrossRef]
33. Otomo, R.; Tatsumi, T.; Yokoi, T. Beta zeolite: A universally applicable catalyst for the conversion of various types of saccharides into furfurals. *Catal. Sci. Technol.* **2015**, *5*, 4001–4007. [CrossRef]
34. Chang, C.D.; Silvestri, A.J. The conversion of methanol and other O-compounds to hydrocarbons over zeolite catalysts. *J. Catal.* **1977**, *47*, 249–259. [CrossRef]
35. Osuga, R.; Yokoi, T.; Kondo, J.N. Probing the basicity of lattice oxygen on H-form zeolites using CO_2. *J. Catal.* **2019**, *371*, 291–297. [CrossRef]
36. Schröder, K.P.; Sauer, J. Preferred stability of aluminum-oxygen-silicon-oxygen-aluminum linkages in high-silica zeolite catalysts: Theoretical predictions contrary to Dempsey's rule. *J. Phys. Chem.* **1993**, *97*, 6579–6581. [CrossRef]
37. Groen, J.C.; Peffer, L.A.A.; Moulijn, J.A.; Pérez-Ramírez, J. On the Introduction of Intracrystalline Mesoporosity in Zeolites Upon Desilication in Alkaline Medium. *Micropor. Mesopor. Mater.* **2004**, *69*, 29–34. [CrossRef]
38. Podolean, I.; Dogaru, M.; Guzo, N.C.; Petcuta, O.A.; Jacobsen, E.E.; Nicolaev, A.; Cojocaru, B.; Tudorache, M.; Parvulescu, V.I.; Coman, S.M. Highly Efficient Ru-Based Catalysts for Lactic Acid Conversion to Alanine. *Nanomaterials* **2024**, *14*, 277. [CrossRef]
39. Petcuta, O.; Guzo, N.; Parvulescu, V.I.; Coman, S.M. *Bifunctional Ru/Beta Zeolite Catalysts for the Biomass Feedstock Upgrading*; BioMat Proceedings Book; NTNU: Trondheim, Norway, 2022; Available online: https://chimie.unibuc.ro/edu/greencam/index.php/summer-school-2022 (accessed on 1 November 2024).
40. Liu, J.; Lee, J.B.; Kim, D.H.; Kim, Y. Preparation of high concentration of silver colloidal nanoparticles in layered laponite sol. *Colloids Surf. A* **2007**, *302*, 276–279. [CrossRef]
41. Balcerzak, J.; Redzynia, W.; Tyczkowski, J. In-situ XPS analysis of oxidized and reduced plasma deposited ruthenium-based thin catalytic films. *Appl. Surf. Sci.* **2017**, *426*, 852–855. [CrossRef]
42. Jae, J.; Tompsett, G.A.; Foster, A.J.; Hammond, K.D.; Auerbach, S.M.; Lobo, R.F.; Huber, G.W. Investigation into the shape selectivity of zeolite catalysts for biomass conversion. *J. Catal.* **2011**, *279*, 257–268. [CrossRef]
43. Al-Shaal, M.G.; Wright, W.R.H.; Palkovits, R. Exploring the ruthenium catalysed synthesis of γ-valerolactone in alcohols and utilisation of mild solvent-free reaction conditions. *Green Chem.* **2012**, *14*, 1260–1263. [CrossRef]
44. Wei, Z.; Li, X.; Deng, J.; Wang, J.; Li, H.; Wang, Y. Improved catalytic activity and stability for hydrogenation of levulinic acid by Ru/N-doped hierarchically porous carbon. *Mol. Catal.* **2018**, *448*, 100–107. [CrossRef]
45. Shao, Y.; Wang, J.; Sun, K.; Gao, G.; Li, C.; Zhang, L.; Zhang, S.; Xu, L.; Hu, G.; Hu, X. Selective hydrogenation of furfural and its derivative over bimetallic NiFe-based catalysts: Understanding the synergy between Ni sites and Ni–Fe alloy. *Renew. Energy* **2021**, *170*, 1114–1128. [CrossRef]
46. Weng, R.; Yu, Z.; Xiong, J.; Lu, X. Effects of water in the heterogeneous catalytic valorization of levulinic acid into γ-valerolactone and its derivatives. *Green Chem.* **2020**, *22*, 3013–3027. [CrossRef]
47. Velisoju, V.K.; Peddakasu, G.B.; Gutta, N.; Boosa, V.; Kandula, M.; Chary, K.V.R.; Akula, V. Influence of Support for Ru and Water Role on Product Selectivity in the Vapor-Phase Hydrogenation of Levulinic Acid to γ-Valerolactone: Investigation by Probe-Adsorbed Fourier Transform Infrared Spectroscopy. *J. Phys. Chem. C* **2018**, *122*, 19670–19677. [CrossRef]
48. Zhang, L.; Chen, K.; Chen, B.; White, J.L.; Resasco, D.E. Factors that Determine Zeolite Stability in Hot Liquid Water. *J. Am. Chem. Soc.* **2015**, *137*, 11810–11819. [CrossRef]
49. Pinto, B.P.; Fortuna, A.L.L.; Cardoso, C.P.; Mota, C.J.A. Hydrogenation of Levulinic Acid (LA) to γ-Valerolactone (GVL) over Ni–Mo/C Catalysts and Water-Soluble Solvent Systems. *Catal. Lett.* **2017**, *147*, 751–757. [CrossRef]
50. Jiang, L.; Xu, G.; Fu, Y. A nitrogen-doped carbon modified nickel catalyst for the hydrogenation of levulinic acid under mild conditions. *Green Chem.* **2021**, *23*, 7065–7073. [CrossRef]
51. Hernando, H.; Moreno, I.; Fermoso, J.; Ochoa-Hernández, C.; Pizarro, P.; Coronado, J.M.; Čejka, J.; Serrano, D.P. Biomass catalytic fast pyrolysis over hierarchical ZSM-5 and Beta zeolites modified with Mg and Zn oxides. *Biomass Convers. Bioref.* **2017**, *7*, 289–304. [CrossRef]
52. Zeng, W.; Cheng, D.-G.; Chen, F.; Zhan, X. Catalytic Conversion of Glucose on Al–Zr Mixed Oxides in Hot Compressed Water. *Catal. Lett.* **2009**, *133*, 221–226. [CrossRef]

53. Groen, J.C.; Moulijn, J.A.; Pérez-Ramírez, J. Alkaline posttreatment of MFI zeolites. From accelerated screening to scale-up. *Ind. Eng. Chem. Res.* **2007**, *46*, 4193–4201. [CrossRef]
54. Aireddy, D.R.; Ding, K. Heterolytic Dissociation of H_2 in Heterogeneous Catalysis. *ACS Catal.* **2022**, *12*, 4707–4723. [CrossRef]
55. Coman, S.M.; Parvulescu, V.I. Heterogeneous Diastereoselective Catalysis—A Powerful Strategy Toward C(15) Stereoselectivity from PGF2α Analogues Structure. *Curr. Pharm. Des.* **2015**, *21*, 5558–5572. [CrossRef] [PubMed]
56. Ruppert, A.M.; Grams, J.; Jedrzejczyk, M.; Matras-Michalska, J.; Keller, N.; Ostojska, K.; Sautet, P. Titania-Supported Catalysts for Levulinic Acid Hydrogenation: Influence of Support and its Impact on γ-Valerolactone Yield. *ChemSusChem* **2015**, *8*, 1538–1547. [CrossRef]
57. Pârvulescu, V.; Coman, S.; Palade, P.; Macovei, D.; Teodorescu, C.; Filoti, G.; Molina, R.; Poncelet, G.; Wagner, F. Reducibility of ruthenium in relation with zeolite structure. *Appl. Surf. Sci.* **1999**, *141*, 164–176. [CrossRef]
58. Bhat, R.N.; Kumar, R. Synthesis of zeolite beta using silica gel as a source of SiO_2. *J. Chem. Technol. Biotechnol.* **1990**, *48*, 453–466. [CrossRef]
59. Zhang, Q.H.; Gao, L.; Guo, J.K. Effects of calcination on the photocatalytic properties of nanosized TiO_2 powders prepared by $TiCl_4$ hydrolysis. *Appl. Catal. B* **2000**, *26*, 207–215. [CrossRef]
60. Teodorescu, C.M.; Esteva, J.M.; Karnatak, R.C.; El Afif, A. An approximation of the Voigt I profile for the fitting of experimental X-ray absorption data. *Nucl. Instrum. Methods Phys. Res. Sect. A—Accel. Spectrom. Dect. Assoc. Equip.* **1994**, *345*, 141–147. [CrossRef]
61. Mardare, D.; Luca, D.; Teodorescu, C.M.; Macovei, D. On the hydrophilicity of nitrogen-doped TiO_2 thin films. *Surf. Sci.* **2007**, *601*, 4515–4520. [CrossRef]